



# Feedbacks between fast brittle faulting, hydrothermal fluid flow, and metal transport within carbonated ultramafics (Ligurian Western Alps, Italy)

Paolo S. Garofalo<sup>1</sup> · Marco Scarsi<sup>2</sup> · Alexander Gundlach-Graham<sup>3,4</sup> · Gunnar Schwarz<sup>3</sup> · Detlef Günther<sup>3</sup>

Received: 25 March 2021 / Accepted: 29 September 2022  
© The Author(s) 2022

## Abstract

The Bisciarelle fault is a brittle thrust crosscutting lherzolite of the Voltri Massif (Italy) and is similar to the historical gold veins of the area. This is a 16-m-thick fault showing a large damage zone and a 4-m-wide hydrothermal alteration halo. Its fault rocks interacted with a hydrothermal fluid and host peculiar Au-bearing zones made of concentric and circular dolomite aggregates, which we call spherulites, and chalcedony. To constrain spherulite genesis, we quantify fluid-fault interactions at Bisciarelle combining field and microtextural data, mass transfer calculations, and a multi-technique analytical dataset including element imaging by laser ablation-inductively coupled plasma-time-of-flight mass spectrometry. We show that faulting was coupled with significant transfer of H<sub>2</sub>O, CO<sub>2</sub>, Ca, Sb, and W from the fault fluid to the protolith, and variable transfers of SiO<sub>2</sub> and some trace elements from the protolith to the fluid. This process deposited Au within the spherulites, caused serpentinization and carbonation of the protolith, and weakened the fault localizing subsequent shearing events and providing components for the growth of spherulites and the other fault rocks.

We interpret Bisciarelle as a permeable epizonal orogenic vein, which formed fast as a result of dilation and top-to-NE shearing. This fault developed via cycles of fluid pressure build-up, opening, fluid effervescence, and mineral precipitation from a H<sub>2</sub>O-CO<sub>2</sub> hydrothermal fluid. The fluid transported and deposited a suite of metals including Au and interacted with the protolith. A similar mechanism of faulting and reactive fluid flow could have generated the other Au deposits of the area.

**Keywords** Fluid–rock interaction · Voltri massif · Orogenic deposits · Laser ablation–inductively coupled plasma–time-of-flight mass spectrometry (LA-ICP-TOFMS) · Elemental imaging

## Introduction

It is commonly accepted that fault zones act as hydrothermal fluid conduits within the crust. Fluid transmissive fault zones generate veins (Oliver and Bons 2001) and are important loci of ore deposition in a number of geological environments (e.g., Cowan 2020; Foxford et al. 2000). These faults and their associated veins may show a gamut of textures at the meso- and micro-scales (e.g., Dong et al. 1995) that are dependent on the extensional, hybrid, or shear nature of the fault and on fluid pressure (Bons et al. 2012). There is therefore a close feedback between failure modes of fault zones, their fabric, hydrothermal fluid flow, and vein formation, all of which are mutually dependent and steer ore formation.

Hydrothermal fluids within fault zones may modify the mineralogical, chemical, and textural properties of the protolith during deformation. This modification is carried out by the precipitation of minerals within the zone, which might

---

Editorial handling: F. Melcher.

✉ Paolo S. Garofalo  
paolo.garofalo@unibo.it

- <sup>1</sup> Dipartimento Di Scienze Biologiche, Geologiche Ed Ambientali, Università Degli Studi Di Bologna, Piazza Di Porta S. Donato, 1, 40126 Bologna, BO, Italy
- <sup>2</sup> Dipartimento Di Scienze Della Terra, Dell’Ambiente E Della Vita, Università Degli Studi Di Genova, Corso Europa, 26, 16132 Genoa, GE, Italy
- <sup>3</sup> Laboratory of Inorganic Chemistry, Department of Chemistry and Applied Biosciences, ETH Zurich, Zurich, Switzerland
- <sup>4</sup> Department of Chemistry, Iowa State University, Ames, IA, USA

choke or enhance porosity depending on the type of fluid-fault interaction (Torabi et al. 2020b). Away from a fault zone, fluid-fault interactions may leave cryptic to visible haloes in the protolith (Reed 1997), which can vary along and across fault strike due to the variable composition of fault and wallrock minerals (selvaging: Cathles 1991) or due to distinct fault fluids (Garofalo 2004).

Models were set up as a guide for the evaluation of the structural properties of upper-crustal, brittle fault zones (Caine et al. 1996; Torabi et al. 2020a, and ref. therein). These properties are relevant for the interpretation of the data presented in this study. The architecture of a brittle fault zone (Fig. 1) is ideally made of a fault core and a damage zone, which develop at different times and are made of distinct rocks. The core is a part of a fault that accommodates most of the displacement and that is made of thin slip surfaces, clay-rich gouges, incohesive breccias, and cataclastic/ultracataclastic zones in which the protolith experienced the highest degree of comminution. A damage zone is the heterogeneous part of a fault made of veins, cleavage planes, deformation bands, and other fault rocks that form during multiple episodes of slip. As a general rule, a core develops from a damage zone as a result of deformation and comminution. Its permeability is dominated by grain-scale processes and may show stages of fluid-assisted strain hardening and weakening (e.g., Vignaroli et al. 2020). Fault cores tend to be barriers to fluid flow due to permeability reduction processes, while a damage zone is dominated by the hydraulic permeability of the fracture network (Caine et al. 1996). The presence of a wide damage zone and a relatively thin core causes a brittle fault to act as a conduit for hydrothermal fluid flow, and the presence of a wide core and a thin damage zone generates a localized barrier to flow.

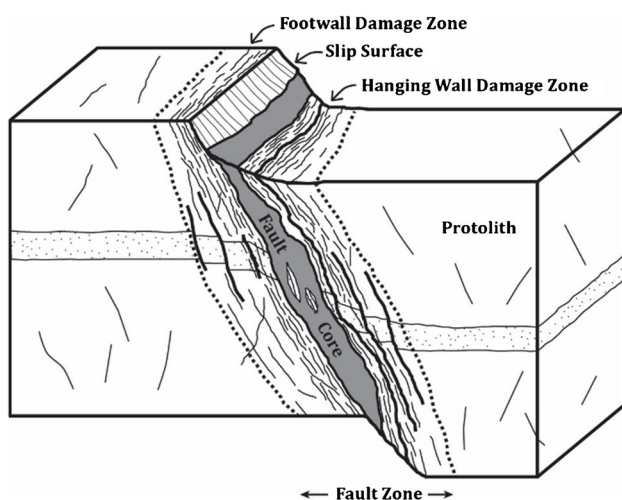


**Fig. 1** Primary structural and lithological components of a brittle normal fault (mod. after: Torabi et al. 2020a). No scalar relationships are implied between these components

Hence, open questions are the differences between the typical upper crustal faults (Fig. 1) and those that host large hydrothermal fluid flow and ore precipitation in terms of fault architecture, fabric, and textures.

In this study, we combine field data with a multi-technique analytical dataset to constrain the processes in an Au-mineralized upper crustal fault. This fault is hosted by serpentinized lherzolite, is enveloped by a wide carbonate hydrothermal alteration halo whose mineral assemblage resembles that of the listwanite, and shows an association of lithologies and fabrics that indicate a high bulk permeability at the time of failure and fluid flow. We focus our attention on the genesis of an Au-bearing, highly permeable zone, which developed synkinematically and shows a peculiar texture made of circular and concentric dolomite aggregates. We propose a link between the structural evolution of the zone and fluid-fault interaction and Au deposition.

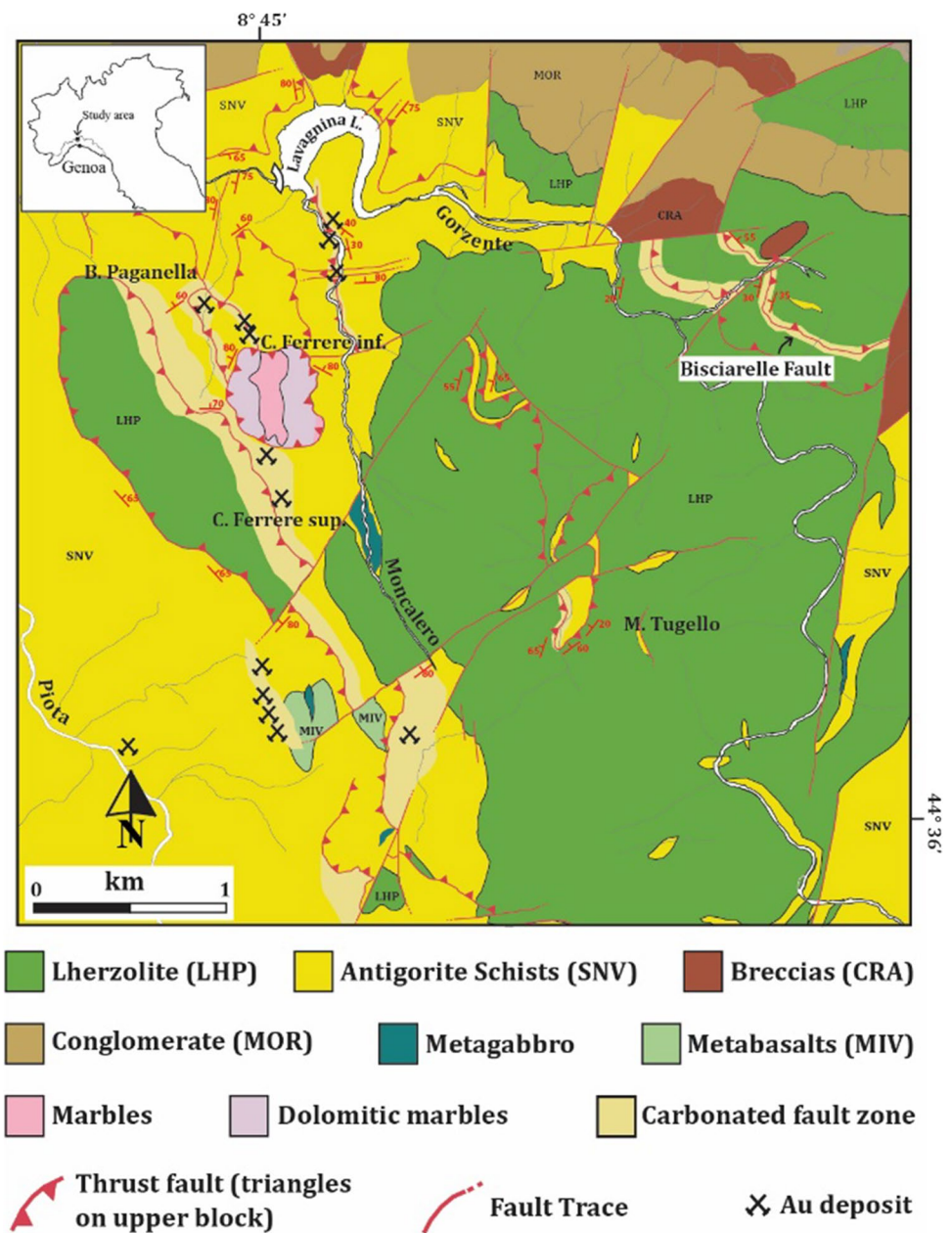
## Geology of the Lavagnina Lakes area

The Lavagnina Lakes (Fig. 2) are located near Casaleggio Boiro (Alessandria, Italy). The area occupies the north-eastern boundary of the Voltri Unit, Ligurian Western Alps (Scarsi et al. 2019), and belongs to a region that is known for Au deposits that are documented from the year 1589 to the end of the nineteenth century (Pipino 2001). A more complete account of the historical Au deposits of the area is provided in the Electronic Supplementary Materials (ESM). The Lavagnina Lakes zone belongs to the ophiolitic complex of the Voltri Massif. It consists of serpentinite associated with metagabbro, mafic metavolcanics, metasediments, and lherzolite associated with minor pyroxenite and dunite bodies. The Massif experienced an Alpine tectono-metamorphic history including the ductile and brittle regimes (Capponi and Crispini 2002, and ref. therein), and from high-pressure metamorphic conditions to variable retrogressive greenschist overprints (Scarsi et al. 2018).

The most abundant lithologies of the Lavagnina Lakes (Fig. 2) are peridotite of the Voltri Unit (also: Erro-Tobbio Unit), continental breccias, and conglomerates of the Tertiary Piedmont Basin. The peridotite consists mainly of lherzolite with minor dunitic lenses, showing degrees of serpentinization and slices of metagabbro and mafic metavolcanics. In the studied area, serpentinized lherzolite shows a transitional contact with serpentine schists.

The structural evolution of the area is made of several superimposed deformation events, which occurred under a tectonic regime evolving from brittle-ductile to brittle. The oldest Alpine structures of the area can be referred to the ductile D1-D2 deformation stages (Capponi and Crispini

**Fig. 2** Geological sketch map of the Lavagnina Lakes and Bisciarelle fault area (modified after: Pipino 2003; Scarsi et al. 2019)



2002). The following stages generated a complex superposition of ductile, brittle-ductile, and brittle structures that developed at higher structural levels and are represented by different sets of folds, reverse shear zones, and fault systems. Upper crustal faults are common in the Lavagnina Lakes zone and form sets of reverse shear zones (RSZ 2) that host Au-mineralized vein networks and associated wall rock hydrothermal alteration (Giorza 2010). The historical Au deposits and the Bisciarelle fault are shear zones that belong to this category.

## Methods

Field work was conducted to define the structural elements of the Bisciarelle fault and to collect samples of fault rocks and protolith. Ten samples of the host lherzolite (RB1-RB10, Fig. 3a–b) were collected along a 15.6-m profile directed at high angle with respect to the fault strike. A structural log of the fault was constructed based on fabric analysis and thickness measurements (Table 1, ESM). Eighteen samples of core and fault lithologies were used to determine the

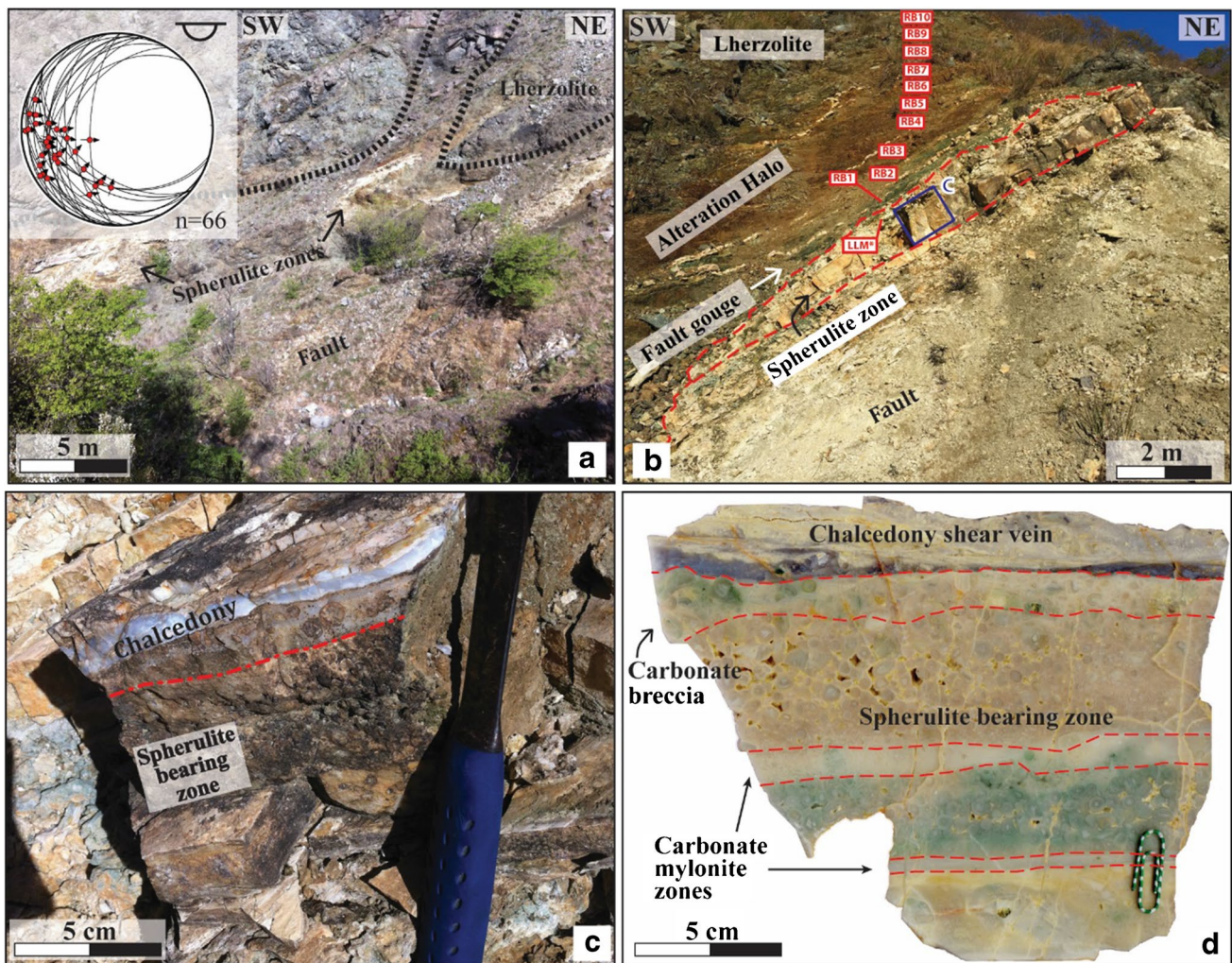


**Fig. 3** Characteristics of the Bisciarelle thrust fault. **a** Field appearance of fault and associated hydrothermal alteration halo. The dotted curve marks the contact between protolith and fault. The position of the largest spherulite levels is indicated. The Schmidt stereonet shows the attitude of fault surfaces (red spots: slickenlines; arrows show the top-to-E/NE sense of shear). **b** Relations between spherulite level, fault gouge, and hydrothermal alteration at the hanging wall of the

fault. The blue rectangle marks the position of the photo in panel d. The RB1 to RB10 labels mark the sampling points of the alteration halo. Sample LLM\* was used for elemental imaging with LA-ICP-TOFMS. **c** Detail of the spherulite level at the contact with two adjacent chalcidony shear veins. **d** Polished slab of the spherulites, chalcidony vein, and secondary shear surfaces

microstructural properties of the fault, mainly carbonated cataclasite, spherulite levels, breccia, and gouge, which were studied in thirty-four polished thin sections. These samples have been studied combining a petrographic study, morphometric analysis of fault core samples, X-ray powder diffraction analysis, SEM-energy dispersive X-ray spectroscopy, whole-rock chemical analyses, and 1-D scan and 2-D chemical analyses by laser ablation-inductively coupled plasma-time-of-flight mass spectrometry (LA-ICP-TOFMS). This last set of analyses followed an established protocol (Burger et al. 2015; Gundlach-Graham et al. 2015), but with distinct operating parameters that lead to different sensitivities. The 2-D element distribution images were constructed using a single-pulse mode, in which laser spot with a 10- $\mu\text{m}$

diameter, a laser shot repetition rate of 25 Hz, and a line scan speed of  $250 \mu\text{m s}^{-1}$  were used to build an image from an array of  $1000 \times 1000$  LA shots. The 1-D scan mode was carried out using a hole-drilling mode (25 pulses per spot), a 5  $\mu\text{m}$  laser spot diameter and a faster repetition rate (100 Hz) to improve the limits of detection by ablating more material per LA spot. This improvement was quantified as c. 1 order of magnitude for most of the light elements, and c.  $\frac{1}{2}$  order of magnitude for the heavy elements including gold (Fig. S14 of ESM). More details on field documentation, descriptions of the analytical techniques used, and pertinent figures of merit for all analytical measurements are provided in the ESM.

**Table 1** Log of the Bisciarelle thrust fault

Fault rock	Thickness (m)	Description
Protolith (hanging wall)		Serpentinites and serpentinite schists, greenish to brownish in color
Carbonated protolith with carbonate veins	10	Serpentinite schists with poorly coherent, intensely foliated domains (at 1, 2.8, and 3.8 m from fault contact). Crosscut by two sets of joints. Close to the fault, they are visibly altered for c. 4 m
Carbonated saponite-bearing gouge	0.5	Gouge made of carbonates and emerald green saponite at contact with spherulite level. Sharp contact
Spherulite- and chalcedony-bearing level	0.7	Two whitish, porous levels of dolomitic spherulites (15 and 20 cm in thickness, respectively) alternating with several chalcedony shear veins (up to 15-cm-thick, sharp contacts). Spherulites are very well rounded, range from mm to cm in diameter, and make up to 80 vol% of rock. Slicken lines and chatter marks (5–6 cm long) dip to W-NW and show a top-to-NE sense of shear. Quartz injection veins
Cockade breccia	0.2	Cockade breccia (cf. Genna et al. 1996) with angular clasts (cm in size) made of serpentinite and carbonated serpentinites (up to 50 vol%). Matrix made of crystalline carbonates. Sharp contacts with spherulite level. Clast dimensions increase towards the footwall, and are coupled with a decrease of volume of carbonatic matrix
Limestone	0.3	Whitish, crystalline, and massive limestone
Carbonated fault gouge	1.5	Greenish, carbonated fault gouge (cf. Sibson, 1977) made of serpentinite clasts (< 4 mm in size, c. 25 vol%), which are randomly oriented inside a carbonated serpentinite matrix (c. 75 vol%)
Carbonated cataclasites	1.5	Greenish carbonated cataclasites made of serpentinite clasts (mostly 4–5 cm in size, 40–50 vol%), which are randomly oriented inside a carbonated-serpentinite matrix (< 50–60 vol%)
Duplex structures	0.2	Whitish saponite level with sigmoidal fabric showing top-to-NE sense of shear
Cataclasites/ultracataclasites	3.0	Dark-green to brownish cataclasites made of serpentinite clasts (few mm in size) that are well rounded and sorted (40–50 vol%) and set in a reddish, carbonate microcrystalline matrix (50–60 vol%). Whitish ultracataclasite made of randomly oriented, angular serpentinite clasts (< 1 cm in size). These clasts (5–10 vol%) are surrounded by a reddish, microcrystalline carbonate matrix (up to 90–95 vol%)
Breccias	0.3	Greenish-whitish, hydraulic breccias (cf. Jébrak et al., 1997) with angular to sub-angular serpentinite clasts (cm-dm in size), which are set in a whitish carbonate matrix. Clast size decreases towards the footwall, while proportion of matrix increases
Veined serpentinites	c. 4	Serpentinites and serpentinite schists, brownish in color especially along the pervasive schistosity. Show cm-thick carbonate-chalcedony extensional veins, which cut the schistosity and are randomly oriented. These veins are in turn cut by sigmoidal duplex structures indicating a top-to-NE sense of shear

Notes: fault rocks logged starting from hanging wall. Notice that the undeformed footwall protolith does not outcrop in the area

Mass transfer calculations were based on the multisample, immobile element approach of MacLean and Kranidiotis (1987) and Garofalo (2004; 2012). With this method, the concentrations of rock components are measured along a profile of an alteration zone and plotted in pairs to determine their behavior during alteration. A straight line connecting the origin of binary plots with the least altered sample (protolith) represents the expected trend of a pair of components if both are immobile, i.e., their ratio remains constant within the rock mass. Consequently, the evidence for several pairs of geochemically unrelated components of a rock mass showing linear trends at constant ratios and passing through the origin identifies a set of immobile components (Garofalo 2004, 2012). These components can be subsequently used to calculate mass factors and mass transfers between

protolith and altered rocks. In the ten RB1-RB10 samples, mass transfers have been calculated for all rock components using the expression:

$$\Delta C_i = (C_i^A MF_x) - C_i^O$$

where  $\Delta C_i$  is the mass of component  $i$  exchanged per unit mass of protolith (reported as g/100 g or g/t),  $C_i^A$  is the mass fraction of  $i$  in the considered altered sample,  $C_i^O$  is the mass fraction of  $i$  in the protolith (sample RB10), and  $MF_x = C_{Al_2O_3}^O / C_{Al_2O_3}^x$ . The  $MF_x$  factor is the ratio between the mass fraction of  $Al_2O_3$  in the protolith and that of  $Al_2O_3$  in a given sample  $x$ , as  $Al_2O_3$  has been determined as quasi-immobile. Compositional data and results of mass transfer calculations are reported in the ESM Tables S6 and S7.

## Results

### Field data

The Bisciarelle thrust (44°36'05" N, 8°47'03" E, Fig. 2) strikes NE-SW and outcrops for about 100 m close to the transitional contact between serpentized lherzolite and serpentinite. It dips to the W-SW at c. 20–25°, and has a top-to-NE sense of shear (Fig. 3a). The serpentized lherzolite of the hanging wall has a thickness of more than 10 m, but it is visibly altered close to the contact for a thickness of about 4 m. The fault has a measured thickness of c. 16 m and is made of a number of distinct lithologies (Table 1, ESM Fig. S1–S6). Its true thickness is higher considering the lack of exposure of the footwall lherzolite.

The hanging wall serpentinite schists contain three poorly coherent and intensely foliated domains located at about 1, 2.8, and 3.8 m from the fault core. Closer to the fault contact, a system of extensional carbonate veins develops along the schistosity of the altered rock (Fig. 3a; ESM Figs. S1–S2). They strike mostly sub-parallel to the fault, are up to 2–3 cm in thickness, and dip gently to the NW. The 50-cm-thick visible alteration halo is made of an emerald green to reddish-brown, dolomite-serpentine schist that grades into the outer serpentized lherzolites. This rock is intensely foliated, shows millimetric bands, and its reddish-brown color increases in intensity towards the fault contact, suggesting a coeval development of fault deformation and protolith alteration.

The fault rocks that are adjacent to this gouge show transitional or sharp contacts, and make a complex architecture (Table 1). They are a sequence of (a) cataclasites/ultracataclasites in which serpentinite clasts are set in a crystalline carbonate-rich matrix; (b) hydraulic (cf. Jébrak 1997) and cockade (cf. Genna et al. 1996) breccias made of angular serpentinite clasts set in a carbonate matrix; (c) carbonated serpentinite gouge and saponite-bearing duplex structures; (d) spherulite-bearing zones associated with chalcedony veins and massive and cohesive limestone. The thickness of these fault rocks varies between 20 cm and 3 m, and the clay-rich gouges and duplex structures are located at several positions in the fault architecture.

Towards the footwall, the fault rocks grade into veined serpentinite in which patches of foliated, altered, and brownish schists alternate with patches of less altered serpentinite. Randomly oriented, carbonate-chalcedony extension veins having a thickness of few centimeters and cutting the schistosity, combined with the presence of thin, sigmoidal shear zones, show that this serpentinite represents the footwall damage zone of the thrust fault, and not the undeformed protolith. The lack of footwall protolith makes the evaluation of the true thickness of this damage zone difficult.

The most peculiar rocks of the Bisciarelle fault are two gently dipping dolomitic spherulite-bearing zones, which

are c. 70 and 20 cm in thickness, discontinuous along strike (Fig. 3a, ESM Fig. S1b), and in sharp contact with the emerald-green saponite gouge. The spherulites (Fig. 3c, d) are distinctly round and have a concentric texture and are set in a porous, fine grained but crystalline matrix. Chalcedony shear veins have a maximum thickness of 15–20 cm, a milky color, and show a banded textures. They may crosscut the spherulite zones; however, the evidence that individual spherulites are cut by — but also overgrow — chalcedony indicates that spherulite growth was essentially coeval with shear deformation.

### Protolith petrographic data

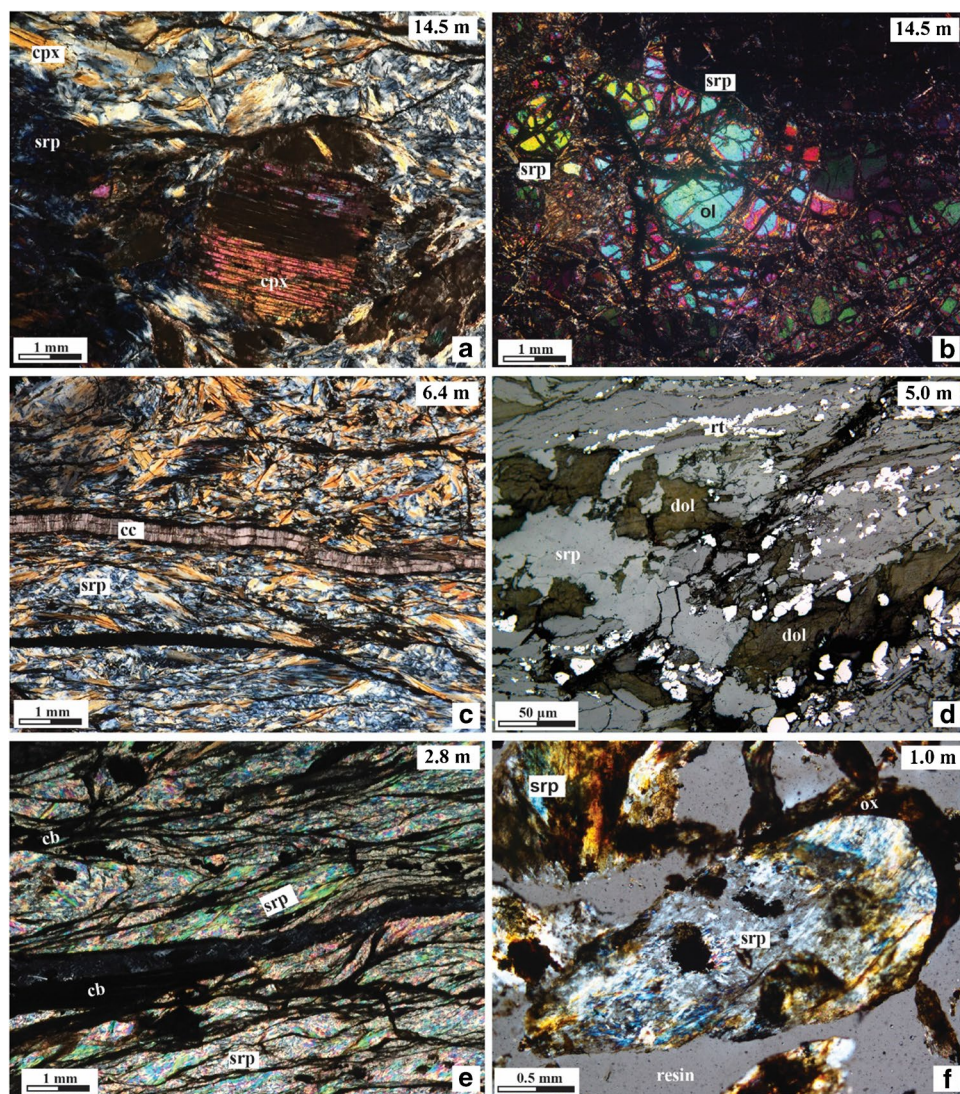
The unaltered lherzolite protolith (Fig. 4a, b) shows a typical orthopyroxene, clinopyroxene, olivine, serpentine, rutile, and ilmenite assemblage. Distinct textural domains are identified, i.e., those in which ortho- and clino-pyroxenes are partially replaced by serpentine from the edges and the cleavage planes (Fig. 4a), domains made of serpentine with mesh textures and olivine core (Fig. 4b), and serpentine-rich domains with bastite texture after ortho- and clino-pyroxene replacement. Serpentine occurs also in secondary veins that cut all the previous textures.

At a distance of 6–7 m from the fault contact there is a transition from lherzolite to serpentinite and serpentinite schists. The serpentinite shows a foliation boudinage, along which most of the minerals are oriented. Remnants of ortho- and clino-pyroxenes are rotated along the foliation (Fig. 4c), and so are ilmenite, rutile (Fig. 4d), and newly formed extensional antitaxial carbonate veins (Fig. 4c, up to 0.2 mm in thickness). In this part of the host rock, the modal abundance of ilmenite and rutile increases considerably.

Between about 6.5 and 3 m from the core (RB7–RB4, cf. Fig. 3b), the serpentinite develops a penetrative foliation similar to a mylonitic texture. Serpentine microlithons alternate with a thin network of authigenic microcrystalline carbonate (Fig. 4e), and ortho- and clino-pyroxenes of the metaperidotite are almost completely replaced by serpentine. In this part of the external zone, the microtextural characteristics of the schists are progressively turned into those of a fault gouge. At a distance of c. 1 m from the fault zone contact (RB2, Fig. 4f), the rock becomes a non-cohesive aggregate of angular to sub-angular serpentinite clasts. The clasts preserve an intense internal foliation, along which dolomite is associated to rutile, ilmenite, and minor pyrite.

The rock immediately adjacent to the fault core (RB1) is a poorly coherent carbonate zone. It is a cataclasite in which fine-grained, sub-angular to well round, randomly oriented dolomite grains are surrounded by saponite, which forms a dark felt around the dolomite. The foliation of this rock is visible at the meso-scale but is lost at the microscale, as only

**Fig. 4** Characteristic textures of the hanging wall protolith at distinct distance from the fault contact. **a** Sample RB10. Clinopyroxenes replaced by serpentine along the crystal edges, with olivine remnants and secondary serpentine veins that cut all the previous textures (cross-polarized light). **b** Sample RB10. Serpentine mesh texture with olivine core (cross-polarized light). **c** Sample RB7. Remnants of pyroxenes rotated along the foliation (cross-polarized light). Extensional anti-taxial carbonate vein develop parallel to the foliation. **d** Sample RB6. Serpentinite with shear zones marked by aggregates of subhedral dolomite and abundant euhedral rutile-ilmenite aligned along the foliation (reflected-light). **e** Sample RB4. Mylonitic texture formed by serpentine microlithons set within a network of microcrystalline carbonate veins, which are present along the schistosity (cross-polarized light). **f** Sample RB2. Serpentinite gouge in which angular to sub angular clasts are set within a serpentine matrix (cross-polarized light). The oxides bordering the serpentine clast armor the clast. Mineral abbreviations follow Whitney and Bernard (2010)



few dolomite veins mark it. Carbonate veins are randomly oriented, up to 0.3 mm in thickness.

### Mass transfer in the damage zone

The chemical composition of the protolith lherzolite (sample RB10) is mostly indistinguishable from that of typical lherzolite of the Voltri Massif (Fig. 5). This is shown mainly by the ratios of the major components (e.g., Al/Ca), which preserve a mantle signature and are identical to those measured in other meta-peridotites (cf. Scambelluri et al. 2001). As a whole, the chemical composition of the undeformed protolith is therefore that of a lherzolite.

In the multisample, immobile element analysis carried out here (Fig. 6), we make the hypothesis that the mineralogical and chemical modification of the protolith took place during one event of interaction with the fault fluid. This model is justified by the evidence for the unaltered lherzolite being

turned progressively into a serpentine-carbonate-ilmenite-rutile schist (Fig. 4c–e) and a serpentinite-saponite fault gouge close to the fault.

Binary compositional plots show that major, minor, and trace components of RB10-RB1 form irregular trends in most cases, i.e., they have variable compositional ratios. This feature is clearly shown by Fig. 6b, e, and f, in which the mass fractions of SiO<sub>2</sub>, MgO, and Fe<sub>2</sub>O<sub>3</sub> are plotted against those of Al<sub>2</sub>O<sub>3</sub>. Lack of linear trends connecting with the origin for the Al<sub>2</sub>O<sub>3</sub>-SiO<sub>2</sub>, Al<sub>2</sub>O<sub>3</sub>-MgO, and the Al<sub>2</sub>O<sub>3</sub>-Fe<sub>2</sub>O<sub>3</sub> pairs implies that they were mobile during hydrothermal alteration (cf. Garofalo 2012). Mobility is shown also by CaO (Fig. 6d) and by the majority of minor and trace elements. Interestingly, the pairs Al<sub>2</sub>O<sub>3</sub>-SiO<sub>2</sub>, Al<sub>2</sub>O<sub>3</sub>-MgO, and Al<sub>2</sub>O<sub>3</sub>-Fe<sub>2</sub>O<sub>3</sub> show trends that correspond quite systematically to large changes in Al<sub>2</sub>O<sub>3</sub> concentrations without corresponding changes in SiO<sub>2</sub>, MgO, and Fe<sub>2</sub>O<sub>3</sub> concentrations. The only sample not following such

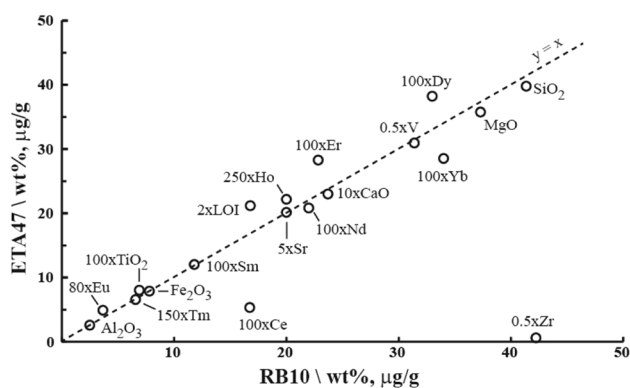


**Fig. 5** Mass fractions of major and minor components of lherzolite RB10 vs. mass fractions of the corresponding components of a typical serpentinized lherzolite from the Erro-Tobbio area (data from: Scambelluri et al. 2001, their Table 1). Mass fractions are scaled to avoid the clustering of data points close to the origin of the axes. The line  $y = x$  is independent from the plotted dataset, and shows the good correlation between the bulk composition of the distal lherzolite of Bisciarelle and that of typical lherzolites of Erro-Tobbio. Among the analyzed components, those that do not follow the correlation are Zr and Ce. In sample RB10, Zr mass fraction (85  $\mu\text{g/g}$ ) is two orders of magnitude higher than that of the typical lherzolites, and Ce (0.18  $\mu\text{g/g}$ ) is three times higher. These features are explained by interaction between the rock and the fault fluid, which introduced the two components within the rock

trend is RB1 from the saponite-bearing gouge. In contrast, the  $\text{Al}_2\text{O}_3$ -LOI (Fig. 6c),  $\text{Al}_2\text{O}_3$ -W (Fig. 6h),  $\text{Al}_2\text{O}_3$ -Sb, and  $\text{Al}_2\text{O}_3$ -Sr pairs show trends that plot systematically above the immobility line on the bulk gain side of the diagram. These trends indicate that the mineralogical and chemical modification of the damage zone took place during removals and additions of  $\text{SiO}_2$ , MgO, and  $\text{Fe}_2\text{O}_3$  from neighboring portions of the host lherzolite, and during substantial addition of  $\text{CO}_2$ ,  $\text{H}_2\text{O}$ , W, and Sb from an external fluid. Hence, only a small number of chemical components were consistently added to the host lherzolite by the fault fluid.

Importantly, only  $\text{Al}_2\text{O}_3$ ,  $\text{TiO}_2$ , Y, V, Sc, and heavy REEs show mass fractions that co-vary approaching linear trends. This implies that during hydrothermal alteration, only a handful of chemical elements remained immobile. This is exemplified by the  $\text{Al}_2\text{O}_3$ - $\text{TiO}_2$  (Fig. 6g) and  $\text{Al}_2\text{O}_3$ -Y (Fig. 6i) plots, which show that a decrease or increase of  $\text{Al}_2\text{O}_3$  concentration in the rock was coupled with a proportional decrease/increase of Y and  $\text{TiO}_2$ , respectively. The  $\text{Al}_2\text{O}_3$ ,  $\text{TiO}_2$ , and Y concentrations in RB1-RB10 do not follow exactly a path of progressive increase/decrease. We interpret this as a product of both local mass losses and gains occurring in neighboring sections of the protolith.

Clear departures from immobile behavior are shown by the RB1-RB3 samples at 1–2 m from the fault contact (Fig. 6i). Such departures are explained mostly by the increased abundance of mode-I carbonate veinlets (Fig. 3b,

ESM Fig. S2), which correspond to a bulk *mass addition* from an external fluid during fracturing and mineral precipitation (Reed 1997).

The computed mass transfers based on the evidence for  $\text{Al}_2\text{O}_3$  immobility identify the rock components that were gained or lost by a unit mass of lherzolite protolith during fluid-rock interaction. The flat profiles lying on the zero-mass-change line show that the protolith did not experience significant mass transfer during deformation up to c. 10 m from the fault contact. This is the protolith showing clinopyroxene and mesh texture in olivine (Fig. 4ab). Starting from a distance of about 8 m from the contact, the protolith records significant chemical and textural modifications. This is the interval in which  $\text{SiO}_2$  (Fig. 7a), MgO (Fig. 7d),  $\text{Fe}_2\text{O}_3$  (Fig. 7f), CaO (Fig. 7b), and LOI (Fig. 7c) show significant coupled transfers from the fluid to the rock. The sharp gains in  $\text{SiO}_2$ , MgO, and volatiles correspond to the formation of serpentine at the expenses of olivine and pyroxene due to dissolution-precipitation reactions, and the gains in CaO and volatiles correspond to the formation of carbonate veinlets (Fig. 4bc). These gains are quantified between 60 and 140% of the protolith values, and are the best estimate of transfers from the fault fluid to the damage zone. Similar gains are shown also by Sb and W (Fig. 7g, h). This transition between the unaltered and serpentinized/foliated protolith is considered the boundary between the damage zone and the relatively intact protolith. Interestingly, the mass transfer data show that this alteration halo is unlike a listwanite alteration due to the lack of significant K mass transfer in the rock (Halls and Zhao 1995).

The change of mass transfer regime at ca. 2–3 m from the fault contact corresponds to a fault section in which the network of carbonate veinlets is denser, in which several intensely foliated serpentine domains form, and includes the 0.5-m-thick, carbonated saponite-bearing gouge (Table 1, Fig. 3b; Fig. 4f). These transfers should be considered as semi-quantitative due to the difficulty to calculate mass transfers close to the fault. In these rocks, CaO and volatiles are probably gained substantially (we calculated at a proportion > 100% of protolith mass), whereas  $\text{SiO}_2$ , MgO,  $\text{Fe}_2\text{O}_3$ , Cr, and Ni show limited mobility. Significant mobility is shown only by Sb (Fig. 7g), Sr, alkalis (Fig. 7e), and in part W (Fig. 7h), which are gained by the rock.

## Spherulite zones

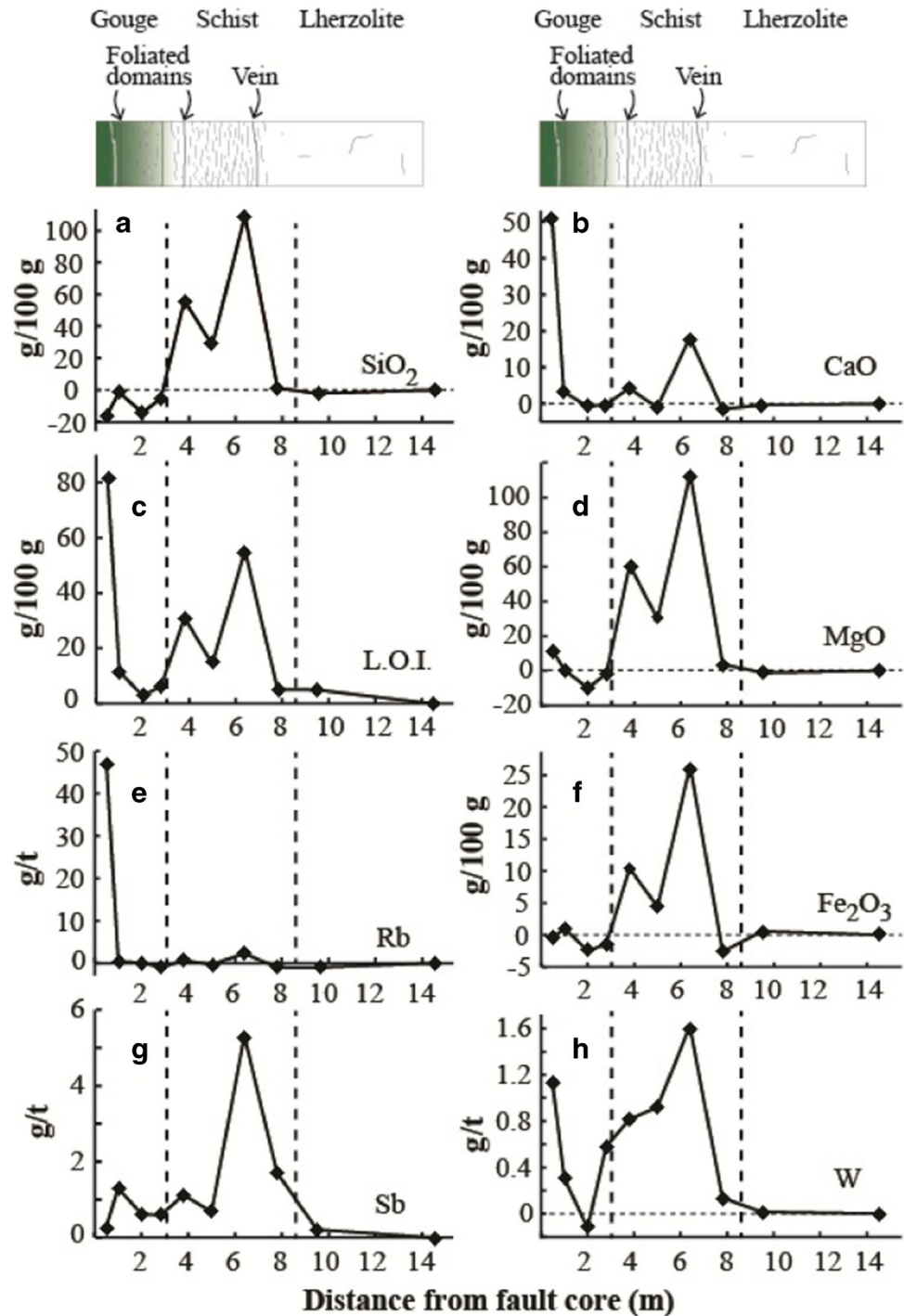
### Petrographic data

Spherulite zones are made of dolomitic spherulites set in a vuggy, fine-grained matrix (Fig. 3c, d; Fig. 8a–c). Individual spherulites are typically not in contact with each other. Morphological analysis demonstrates that large and small spherulites have surprisingly high roundness and circularity,





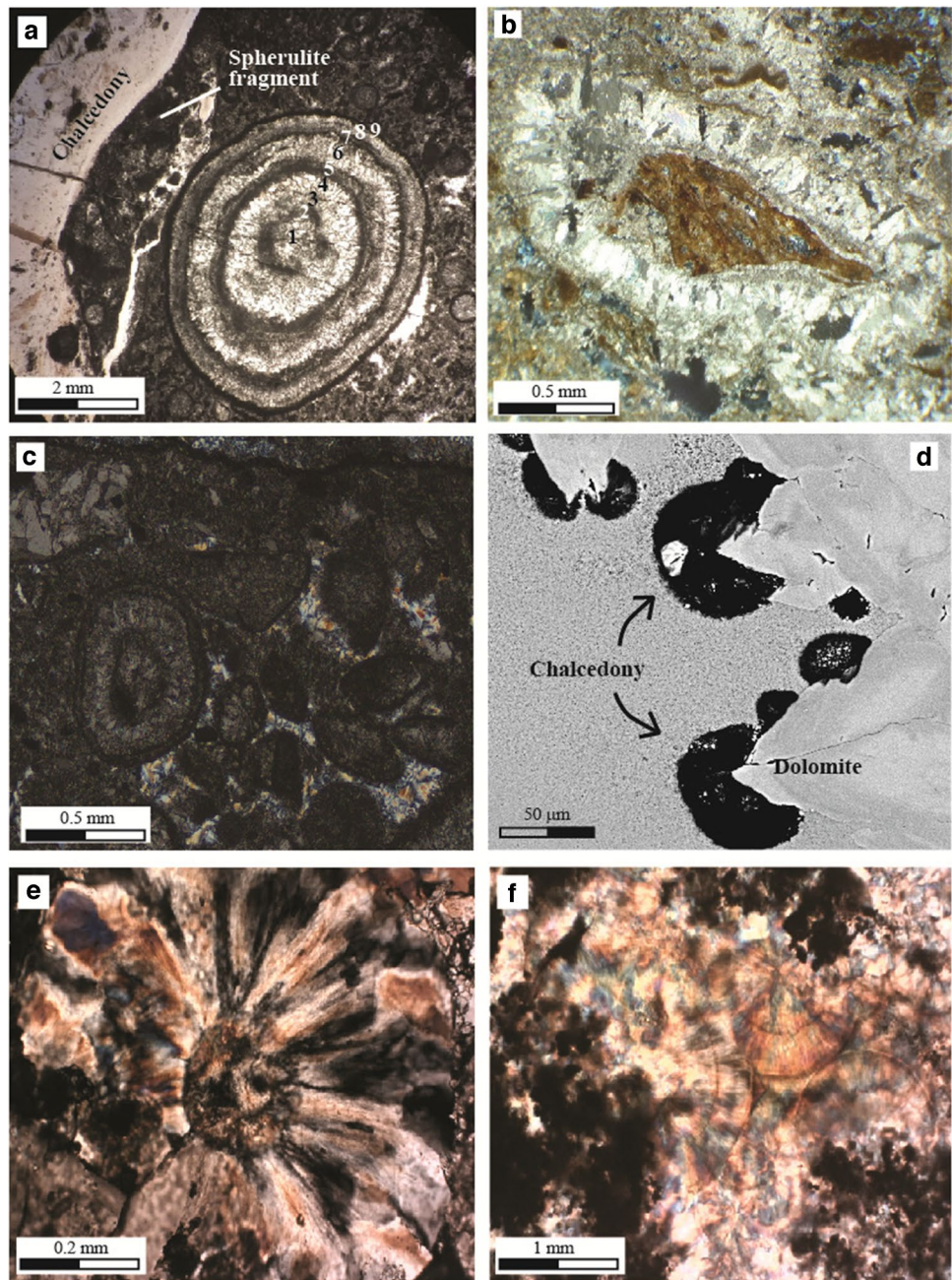
**Fig. 7** Calculated mass transfer profiles of the Bisciarelle fault. The sketches on top of the profiles show the schematic architecture of the fault and its typical fabric, and allow correlation with the calculated profiles



and have an average diameter of 0.5 cm (ESM Fig. S7). A circular shape is found in sections cuts orthogonal and parallel to the slickenlines, indicating that spherulites formed without a preferred orientation with respect to the top-to-NE shear direction of the fault. Single-spot SEM-EDS analyses show that the dolomite has consistently a ferroan dolomitic composition.

Spherulites with a diameter of <2–3 mm are massive, but larger ones may host up to 9 mm thick and show fibrous layers (Fig. 8a). These layers show densely branched dolomite crystals that grow one onto the other from the core, and alternate regularly with dark massive layers having up to 2 mm in thickness. Spherulite cores can be made of altered protolith clasts (Fig. 8b), fragments of fault core breccias, or

**Fig. 8** Characteristic textures of the spherulite zones. **a** Transmitted light photomicrograph of large spherulite with carbonatic core and several concentric bands. **b** Photomicrograph (transmitted light) of small spherulite with a core is made of a carbonated serpentinite fragment. **c** Vuggy chalcidony cementing a group of spherulites. **d** SEM-BSE image of the tips of dolomite crystals from a spherulite band terminating with aggregates of chalcidony spheres, one of which contains a dolomite clast. **e** Photomicrograph (plane polarized light) of a moss recrystallization texture shown by the chalcidony of the spherulite matrix. This texture is made of a round silica core and abutting, radial, and fibrous quartz crystals. **f** Flamboyant textures made of fibrous and radial chalcidony



relicts of carbonated serpentinite clasts. Concentric growth is evident at the meso- micro-scale and show successive layers that depart radially from the cores. Dolomite crystals grow out of the cores without a crystal preferred orientation and terminate abruptly onto the thin, dark layers. In places, delicate spherical aggregates of chalcidony grow attached at the terminations of the dolomite crystals of the spherulite zones (Fig. 8d). Radial growth from the inner core is a strong indication of epitaxial growth (e.g., Pashley 1975), and the arrangement of chalcidony spheres and dolomite crystals indicates undisturbed, hetero-epitaxial growth (Gibson

1988). This demonstrates that the spherulites did not grow competitively in contact with each other.

The chalcidony found in the matrix between the spherulites shows several textures, all of which are typical of open space filling (Moncada et al. 2012, and ref. therein). They are moss (Fig. 8e), fibrous radial, flamboyant (Fig. 8f), and wall lining with central jigsaw textures.

A number of observations shows that, in some places, spherulitic growth in the zones was interrupted by events of cataclasis and micro-brecciation along some secondary slip surfaces (Fig. 8a). These formed angular to sub angular clasts,

which were subsequently recycled as nuclei by following episodes of spherulite growth. Also, carbonate shear zones are found within individual spherulite zones. They are smooth and in general do not crosscut spherulites. The chalcedony shear veins (Fig. 3d) crosscut spherulite zones, but they also overgrow them. This indicates that spherulite formation was essentially coeval with shear deformation. Millimetric breccia veins made of angular to sub-angular carbonate clasts set in chalcedony and quartz matrix are also present.

### Laser Ablation-ICP-Time of Flight Mass Spectrometry

We determined the chemical compositions of spherulite zones and chalcedony by combining line scan analyses of a spherulite by LA-ICP-TOFMS (Fig. 9) with multi-element LA-ICP-TOFMS imaging of a 1 cm<sup>2</sup> area of a spherulite sample (Figs. 10 and 11). Both datasets confirm the single-spot SEM-EDS analyses showing relatively constant Ca and Mg mass fractions within the spherulites; however, they reveal a number of minor and trace components whose mass fractions co-vary significantly together with Ca and Mg. The line scan profile of the spherulite shows flat Ca and Mg mass fractions across the dolomitic layers that *decrease* significantly across the thin, massive layers (layers 1, 2, 3 of Fig. 9a, b). Such decrease is mostly coupled with a significant *increase* in the mass fractions of Fe (Fig. 9c) and a number of trace components (Al, Mn, Cr, Cu, Sb). These coupled variations suggest that the mineralogical composition of the dark thin layers is made of dolomite and a mixture of other phases, but the relative proportion of dolomite is low due to the concomitant deposition of microcrystalline quartz and oxides (Fig. 8a–c). Thus, the thin-massive layers represent stages of spherulite formation in which the epitaxial growth of dolomite was interrupted by the precipitation of a number of metal-rich phases. The evidence for alternation of these deposition stages show that the formation of epitaxial dolomite layers and massive, metal-rich layers repeated cyclically.

In the line scan analyses, Cr, Cu, Rb, Sb, Cs, Ce, Au, and U show mass fractions that are close to the corresponding LODs. These components were determined in a relatively low number of analyses (between c. 10% and 30% of the 534 laser spots across the profile). One of these is Au, which has concentrations within the 0.16–3.5 µg/g range (Fig. 9d). The spatial distribution of Au does not show a systematic occurrence within the dolomite or metal-rich layers. This suggests that Au could be present as micro- (or possibly nano-) inclusions. The high Au mass fractions measured at the end of the scan line profile do not necessarily correspond to spherulite Au, but could set within the microfractures that crosscut the core (Fig. 9a). The high Sb, Co, W, Zn, and Cu mass fractions measured in the same region of the sample are a characteristic of the spherulite banding.

Element imaging by LA-ICP-TOFMS provides a detailed account of the mass fractions of elements within spherulites, matrix, and chalcedony shear veins (cf. Gundlach-Graham et al. 2018; Neff et al. 2020) which provides a gamut of chemical data and a unique complement to mineralogical and petrographic documentation. One striking feature of Figs. 10 and 11 is the presence of a 1-mm-thick fragment of microbreccia at the contact between the spherulite zone and the chalcedony shear vein. This fragment is clearly highlighted by the distribution maps of SiO<sub>2</sub>, CaO, MgO, FeO, MnO, Na, and Sb (Fig. 10), but is less evident in the petrographic photomicrographs (e.g., Fig. 8a).

The thin concentric texture of the large spherulites generates a systematic spatial distribution of major, minor, and trace elements. The thin and massive layers are consistently enriched in Mn, Sr, Co, Pb, Cs, Cr, Y, Ni, Cu, and to a minor degree in SiO<sub>2</sub> and Al<sub>2</sub>O<sub>3</sub>, with respect to the thicker and fibrous dolomite layers, which show only higher mass fractions of FeO (Fig. 10) and W (Fig. 11). The chemical composition of the fine-grained spherulite matrix reflects the texture of its constitutive dolomite and chalcedony. Its most important minor and trace components are FeO, Al<sub>2</sub>O<sub>3</sub>, Sr, Cr, and Cs. Sodium, Cu, Sb, Pb, and U show distinctly higher mass fractions within the matrix.

The chalcedony shear veins host a number of minor and trace components that are disseminated and therefore either replace Si or are inclusions within the solid. The most abundant are Na<sub>2</sub>O and Al<sub>2</sub>O<sub>3</sub> (Fig. 10), but Cr, Co, Pb, Y, and U are present with a lower range of mass fractions. We highlight in particular the 4–18 µg/g range of Sb, which is one of the elements that are gained by the fault protolith (Fig. 7g). The REEs mass fractions are mostly < 2 µg/g in chalcedony (e.g., Ce, Fig. 11), and are at least one order of magnitude higher than those of spherulites and matrix.

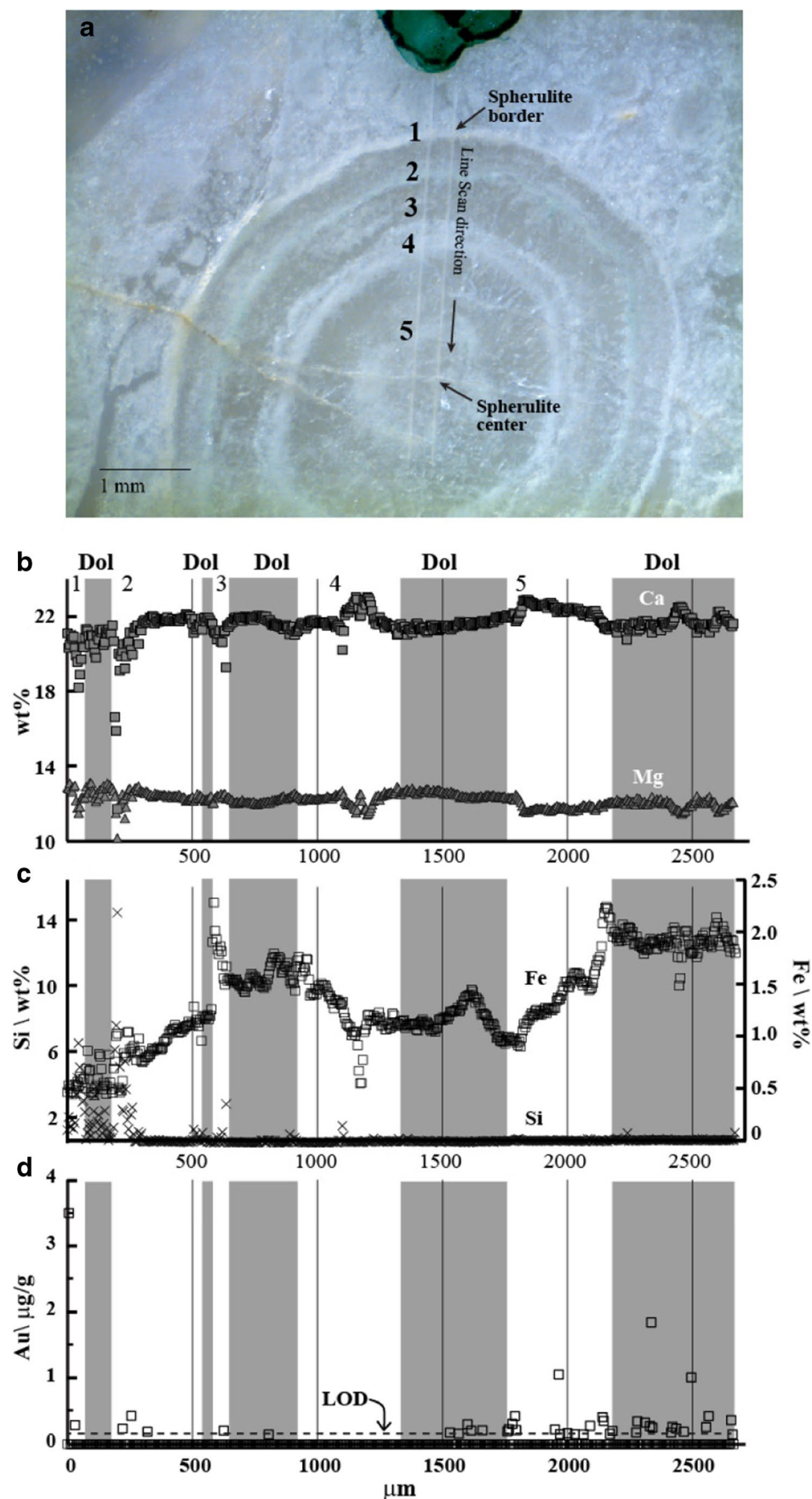
## Discussion

Our data confirm previous works carried out in the Lavagnina Lakes area concluding that the brittle RSZ2 faults hosted the Au deposits of the district (Capponi and Crispini 2002; Federico et al. 2009; Giorza 2010; Spagnolo et al. 2007). Our data provide however a set of additional constraints on the fluid-fault interaction processes.

### Permeability structure of the bisciarelle fault zone

At Bisciarelle, both hanging wall and footwall protoliths show carbonate extension veins that are typical of damage zones (e.g., Caine et al. 1996). Spherulite zones, cockade, and hydrothermal breccias are fault rocks that must have developed under conditions of tensile hydraulic fracturing, i.e., at conditions at which  $P_f \geq \sigma_3 + T_0$ , where  $P_f$ :

**Fig. 9** Compositional profile of a dolomitic spherulite along a 2670-mm-long LA-ICP-TOFMS line scan. **a** Reflected light photomicrograph of the analyzed spherulite after completion of line scan (i.e., 534 adjacent laser pulses). Numbers mark the positions of five thin, massive bands of the spherulite. The levels marked with dark bands are those of dolomitic composition. Thin fractures occur at the core of the spherulite and cause scatter of compositional data. **b, c** Mass fractions of Ca, Mg, Fe, and Si plotted as a function of position in the line scan. In **c**, the ranges of Si and Fe mass fractions are plotted in different scales and at opposite sides of the panel. **d** Mass fractions of Au in the spherulite plotted as a function of position in the line scan and compared with the determined LOD. The majority of measurements give Au mass fractions below the LOD (ca. 160 ng/g), but 37 analyses give mass fractions comprised between c. 250 ng/g and 3.5  $\mu\text{g/g}$



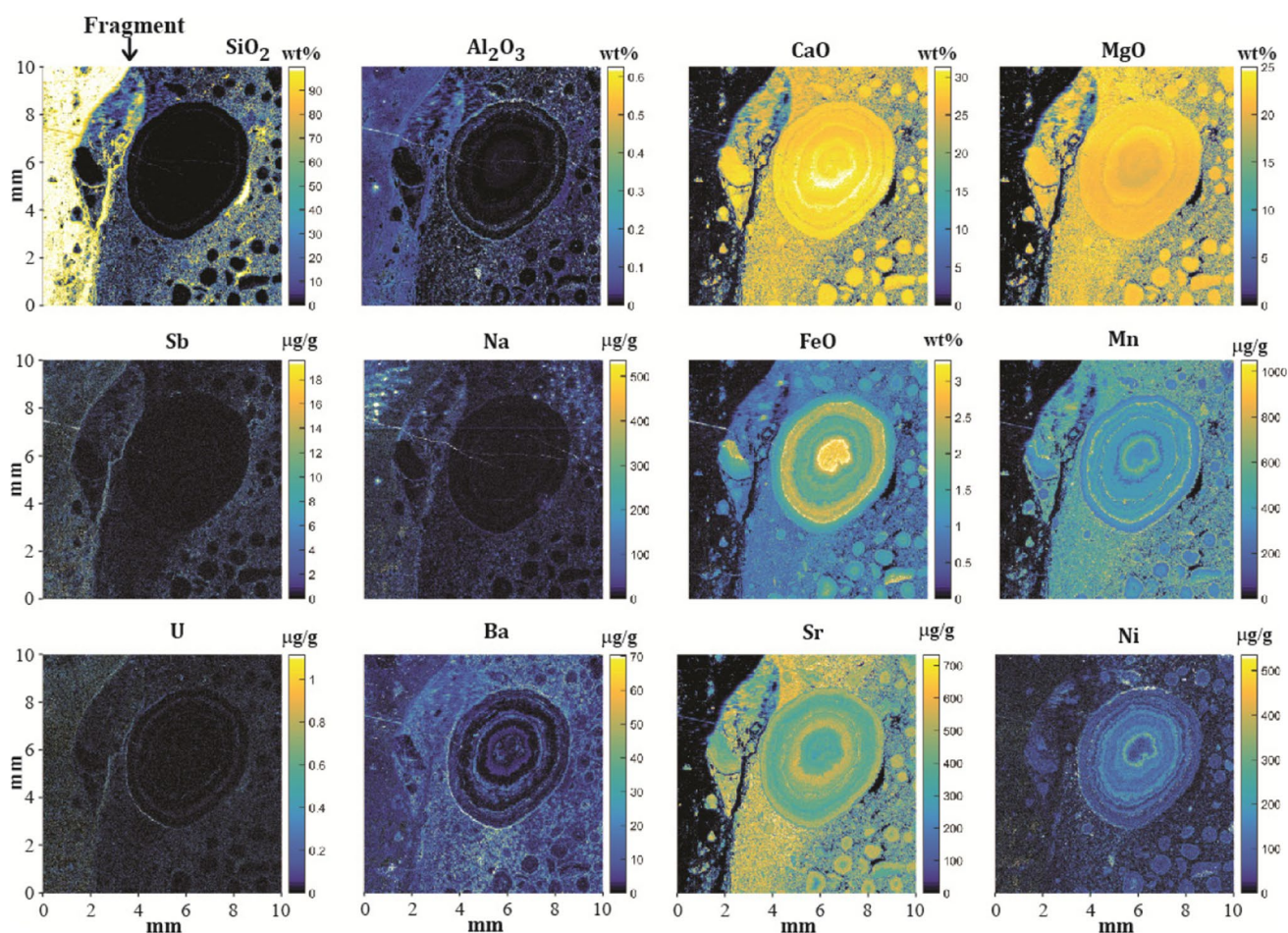


**Fig. 10** Laser ablation-ICP-TOFMS elemental images of a selection of major, minor, and trace components of a spherulite zone and adjacent chalcidony vein. The numbers at the side of the maps show the dimensions of the scanned area, and the color codes correspond to

either wt% oxide or µg/g mass fraction units. The false-color scale of all elemental images span ranges from LOD wt% or µg/g to 99.5% of the maximum value: this scaling provides best image contrast and encompasses most of the mass fraction range

fluid pressure;  $\sigma_3$ : least compressive stress, and  $T_o$ : tensile strength of the rock (Cox et al. 2001). These conditions must have generated high permeability in the damage zone, consistent with the intense hydration and carbonation shown by the mass transfer calculations. This fault section developed probably in a *tensile overpressure state* (Sibson 2017), which in shallow compressional settings like that of Bisciarelle in which  $\sigma_3 = \sigma_v$  is close to lithostatic.

Considering the measured thickness of the fault rocks (Table 1) and the conceptual model of Caine et al. (1996), we calculate that the *maximum* ratio between the damage zone width and the total fault width (architectural index) was equal to about 0.6. This value is expected in transmissive faults that develop within clastic rocks dominated by damage zones, in which deformation is accommodated within localized cataclasites and aquitards are sandwiched between aquifers (Caine et al. 1996). Such value must be considered a maximum estimation because of the impossibility to measure in the field the entire fault thickness. Hence, gouges,

cataclasites, and ultracataclasites localized the shear strain in the Bisciarelle fault, but spherulite zones and breccias constituted the most transmissive segments.

### Fault fluid and spherulite growth

The TP conditions at which deformation took place in the fault cannot be exactly constrained with the data presented here due to the lack of direct geothermometric and geobarometric constraints. However, we follow Giorza (2010) in the hypothesis that the  $H_2O-CO_2$  fluid inclusions ( $X_{CO_2}$ : 0.02–0.03) in the vein Fe-dolomite, magnesite, pyrite, sphalerite, chalcopyrite, and galena (type II veins of Giorza) are representative of the RSZ2 faults. For these inclusions, the entrapment conditions were estimated at 250–300 °C and 7.5–15 MPa.

The spherulite genesis is an intriguing aspect of the structural history of the Bisciarelle fault because is rare in upper crustal faults. The high roundness and circularity, the close packing, the evidence for undisturbed epitaxial growth, the

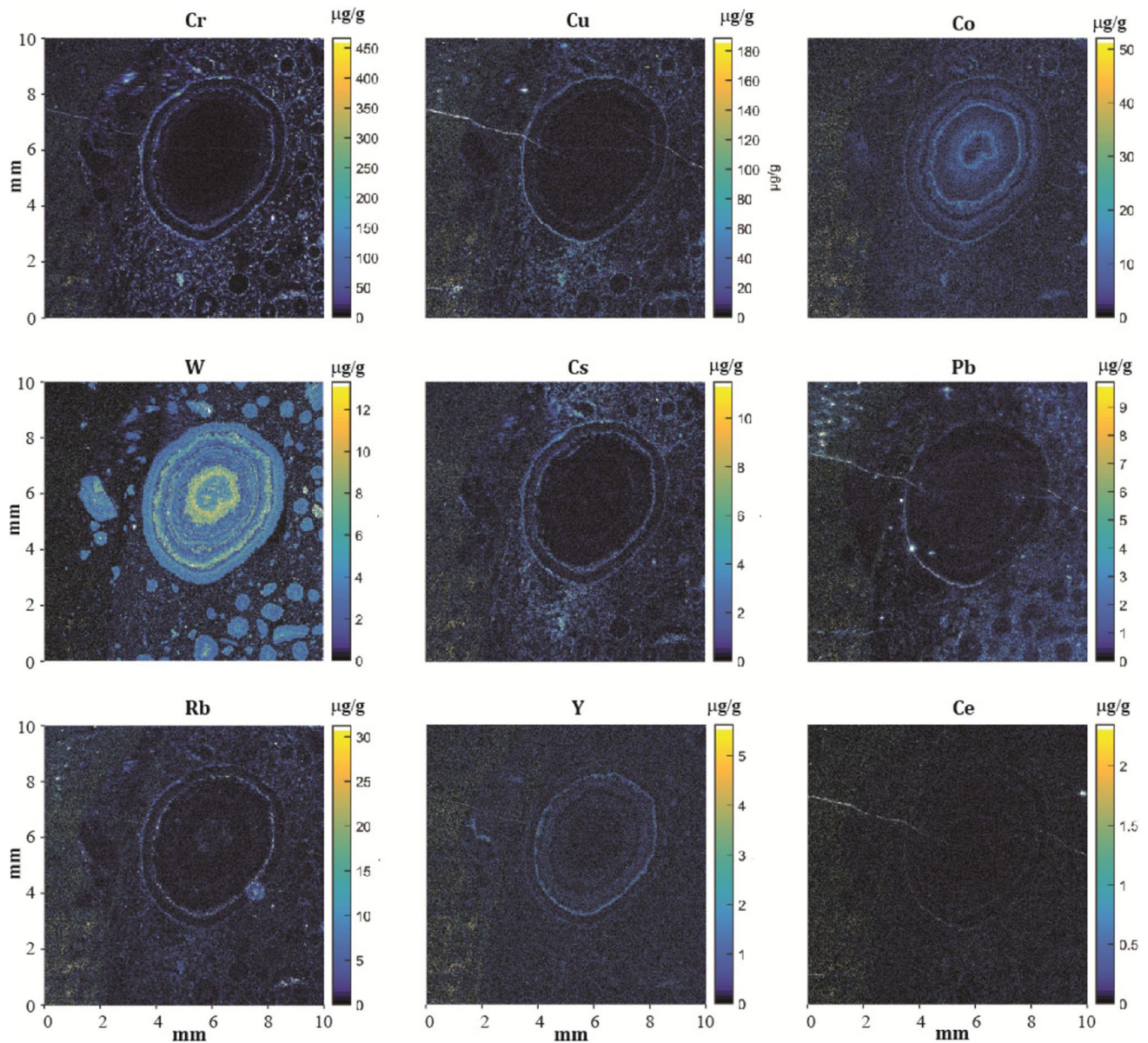


**Fig. 11** Laser ablation-ICP-TOFMS elemental images of a selection of trace components of a spherulite zone and adjacent chalcedony vein (cf. Figure 10)

rhythmic and concentric texture, and their porous and open-space-filling matrix make the spherulites similar to epithermal sinters (Hamilton et al. 2019). We interpret this to indicate that the spherulite zones formed during a combination of dilatation and top-to-NE shearing (hybrid fault failure) at conditions in which the differential stress and  $P_f$  satisfied  $4 < (\sigma_1 - \sigma_3)/T_o < 5.66$  and  $P_f \geq \sigma_3 + T_o$ , respectively. This process must have been cyclic and geologically fast.

Experimental data show that spherulite growth is a fast and non-equilibrium process that is generated by a highly supersaturated fluid (Gránásy et al. 2005; Rodriguez-Blanco et al. 2017). Spherulitic growth proceeds via nucleation of

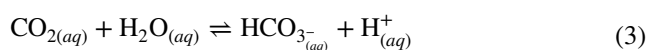
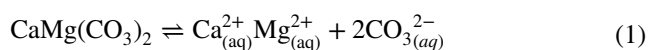
new particles onto a core via non-crystallographic branching, following a process that is called *growth front nucleation* (Gránásy et al. 2005). The round, densely branched spherulites of Bisciarelle belong probably to the *sphere* category of spherulites (Rodriguez-Blanco et al. 2017), for which fast crystallization under high fluid supersaturation is proven experimentally (Andreassen et al. 2010).

Notably, fast growth rates were probably not exclusive of spherulite zones, but occurred also in cockade breccias (ESM Fig. S3, Table 1). Cockade breccias are peculiar rocks proposed to form in suspension within a hydrothermal fluid during cycles of seismic failures of faults (Berger

and Herwegh 2019). These rocks share some characteristics with the spherulites because they show concentric banding around central clasts, open-space filling textures, and sharp boundaries separating clasts and matrix (Frenzel and Woodcock 2014). However, a fundamental difference is that spherulites have small cores (Figs. 3d; 8c, 9a, 10). Also, they lack geopetal indicators, have nearly spherical shapes, and are closely packed with a small volumetric proportion of matrix. These features suggest that while the cockade breccias form after brittle rock failure, disintegration, suspension in a jet of hydrothermal fluid, settling, and agglutination during the interseismic period (Berger and Herwegh 2019), the spherulite zones likely record a shorter sequence of events. They probably grow under a fast, sustained hydrothermal flow that keep them and other clasts in suspension. The evidence for spherulite brecciation and shearing (Figs. 3d and 10) and for brecciated rock fragments at the core of spherulites (Fig. 8b) suggest that episodes of shear deformation and brecciation preceded and followed spherulite formation.

The LA-ICP-TOFMS elemental imaging provides constraints on the mobility of various metals at the time of fluid-fault interaction. Calcium, Sb, W, Sr, and Na are the major and trace constituents of spherulites and matrix (Figs. 10, 11). These components are those that were added in various proportions to the rock during hydrothermal alteration (Fig. 7), indicating that faulting and fluid-mineral equilibria controlled their transfer from the permeable segments of the fault to the protolith. Gold was probably also one of such metals, as the evidence for its determination within the spherulite (0.16–3.5  $\mu\text{g/g}$ , Fig. 9), coupled with its concentration systematically below the LOD of the protolith (2  $\text{ng/g}$ ), indicate that its mobility was restricted within the fault.

Dolomite supersaturation in the fluid must have constrained the genesis of the spherulite zones. We propose that the following simultaneous equilibria provide sufficient constraints on dolomite precipitation:



Important constraints coming from (1) are that dolomite solubility is retrograde with respect to temperature (Fig. 12a), but increases with increasing pressure (Fig. 12b). Thus, a dolomite-saturated fluid at a given T would precipitate dolomite if it is heated or if it decompresses. We

conclude that fluid decompression during a combination of dilatation and shearing of the fault could have been one factor controlling dolomite deposition at Bisciarelle.

A second factor that controlled the precipitation of dolomite in the fault fluid was the Ca/Mg concentration ratio. Experimental data (Rosenberg and Holland 1964) show that in the 250–300 °C interval, dolomite would precipitate from a fluid having  $m_{\text{Ca}^{2+}}/(m_{\text{Ca}^{2+}} + m_{\text{Mg}^{2+}})$  comprised between about 0.72 and 0.94 (Fig. 12c). This is a broad range, which the hydrothermal fluid of Bisciarelle probably met during its flow despite the compositional changes triggered by the mass transfers with the protolith (Fig. 7b, d).

A third factor that controlled the deformation history of the fault must have been the partitioning of  $\text{CO}_{2(\text{aq})}$  into the vapor phase of the fluid as  $\text{CO}_{2(\text{g})}$  (effervescence, or boiling), as described by reaction (2). This partitioning is quantified by the *volatility ratio*, which is calculated as (Drummond and Ohmoto 1985):

$$\text{VR} = m^{\text{V}}/m^{\text{L}}$$

where  $m^{\text{V}}$  and  $m^{\text{L}}$  indicate the molality of the gas species in the vapor and liquid phases, respectively. Between 250 and 300 °C, VR decreases from about 107 to 65, showing that irrespective of the T at which dolomite precipitation took place reaction (2) was driven to the left and that an abundant vapor phase must have been present within the fault. We conclude that at least part of dolomite precipitation at Bisciarelle took place as a result of effervescence of  $\text{CO}_{2(\text{g})}$  from the aqueous fluid experiencing decompression during hybrid opening of the fault. Depending on the starting T, effervescence must have suddenly decreased proton concentration in the fluid by one or more orders of magnitude. As a consequence, this could have driven reactions (3) and (4) to the left, which forced also equilibrium (1) to the left. Effervescence was probably able to cause dolomite precipitation effectively, probably after only 4–5% of exsolution (Drummond and Ohmoto 1985). This process is conceptually similar to that described for the precipitation of hydrothermal calcite in geothermal systems governed by boiling (Simmons and Christenson 1994).

A final aspect to consider in this model is the silica deposition. Hydrothermal silica deposits are typically formed by boiling solutions (Hedenquist et al. 2000) in a proportion that depends on the fraction of the vapor phase at the given temperature. The occurrence of chalcedony veins that are broadly coeval with the spherulites at Bisciarelle, as well as evidence of chalcedony cementing the spherulites, suggests that phase separation could have controlled silica precipitation as well. Experimental data and theoretical considerations for high T hydrothermal fluids show that the addition of  $\text{CO}_2$  in aqueous electrolyte solutions decreases silica solubility considerably, and this tendency increases



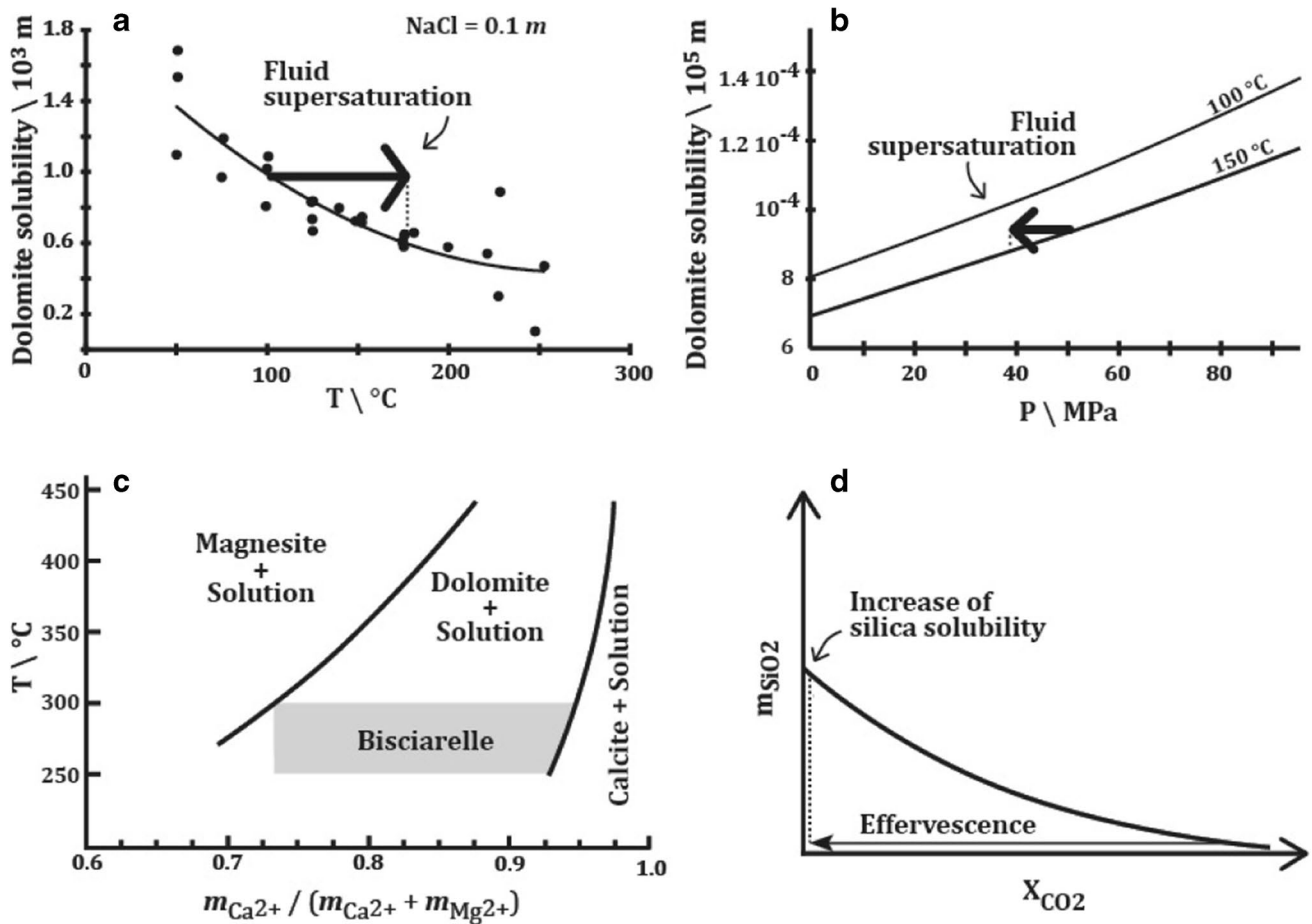


**Fig. 12** Dolomite solubility and processes potentially controlling dolomite precipitation. **a** Experimentally determined solubility of dolomite shown as a function of Mg molality in a H<sub>2</sub>O-NaCl-CO<sub>2</sub> solution (from: Bénézeth et al. 2018). Points are measured solubilities and curve is a best-fit. **b** Dolomite solubility in pure water calculated as a function of fluid pressure and at 100 and 150 °C (from Li et al. 2018). **c** Experimentally determined mole fractions of Ca<sup>2+</sup> and Mg<sup>2+</sup> ions in solution in equilibrium with dolomite+magnesite and dolomite+calcite at T between 275 and 420 °C (from Rosemberg

and Holland, 1964).  $m_{Ca^{2+}}$  and  $m_{Mg^{2+}}$  are the molal concentrations of the Ca<sup>2+</sup> and Mg<sup>2+</sup> ions in solution, respectively. The grey rectangle marks the required fluid composition of the Bisciarelle fluid. **d** Predicted solubility of aqueous silica in equilibrium with quartz and a H<sub>2</sub>O-NaCl-CO<sub>2</sub> fluid expressed as a function of CO<sub>2</sub> concentration and at low-T hydrothermal conditions (modified from: Akinfiev and Diamond, 2009). The solubility is only qualitatively shown because no experimental data are available at 250–300 °C and low P

as a function of CO<sub>2</sub> concentration (Akinfiev and Diamond 2009). In the hypothesis that this process controlled silica solubility also at Bisciarelle (Fig. 12d), the CO<sub>2</sub>-rich fluid could not transport large amounts of silica in solution. However, after phase separation and spherulite formation, an equilibrium shift to the left of (2) must have caused a rapid increase of silica solubility. This increase allowed deposition of chalcedony in veins and matrix. Because the silica deposited by effervescence was the product between the saturation solubility at 250–300 °C and the fraction of water partitioned to the vapor phase (Drummond and Ohmoto 1985), only a proportion of the total silica available in solution formed the chalcedony veins and spherulite matrix.

### Constraints on Au deposition in the Lavagnina Lakes

Our model of the structural evolution of the spherulitic zones of Bisciarelle implies that the damage zone of the fault was the most relevant for hydrothermal fluid flow. This flow occurred during cycles of P<sub>f</sub> build-ups, fault opening, and fluid flushing. Such process must have been fast to allow growth front nucleation of the spherulites and was similar to that described by Sibson et al. (1988) for the fluid-activated valve model. Considering these characteristics, Bisciarelle is an example of *epizonal* orogenic vein (Goldfarb and Groves 2015).

Lack of appropriate outcrops due to exploitation and limited mine documentation complicate a comparison between

Bisciarelle and the historical deposits of the Voltri area. However, the evidence for thick carbonate alteration haloes still visible in the field along the historical outcrops (Fig. 2) suggests that the Au deposits of the area were probably highly permeable faults that experienced intense mass transfer with the ultramafic protolith, similar to what is shown at Bisciarelle. Also, previous studies on orogenic vein textures documented a “spherular” growth of vein quartz of the Voltri deposits (Herrington and Wilkinson 1993, their Fig. 3), suggesting an important similarity with the Biscarelle fault. This implies that a crystallization process similar to the spherulitic growth described in this study could have occurred in the other veins of the network.

The spherular texture was interpreted as a product of crystallization of a pristine amorphous silica, which subsequently recrystallized into quartz, and the presence of a thermodynamically stable form of colloidal Au was postulated in the hydrothermal fluid (Herrington and Wilkinson 1993). Such hypothesis contrasts with the evidence for Au being found mostly as small millimetric nuggets within sulfide (Pipino 1976), which rather indicate that in these deposits Au was transported mainly by sulfide complexes (Seward et al. 2014). However, the detection of Au within the dolomitic spherulites (Fig. 9d) shows that this metal was not transported solely by sulfide complexes, and that additional species must have been stable in the Bisciarelle fluid. These species could be the colloidal Au species, which have been proven to form in quartz-carbonate veins of epithermal deposits as a result of strong decompression and vigorous boiling (McLeish et al. 2021). The formation of such species at the conditions described at Bisciarelle confirms indirectly the model presented here. However, it is unlikely that colloidal species transported significant amounts of Au in the entire vein network of the area.

In addition to the geological and textural similarities between Bisciarelle and the neighbor deposits, fault mineralogy suggests some relevant differences. Bisciarelle was an Au-poor fault of the network made of dolomite, chalcedony, and Mn-Sr oxides, while the historical deposits were Au-rich faults made of a dolomite, magnesite, quartz, chalcedony, and sulfides-sulfosalts (pyrite, chalcocopyrite, pyrrhotite, sphalerite, galena, and tetrahedrite). These distinct assemblages suggest that the ore deposits were generated by a H<sub>2</sub>S-bearing ore fluid capable to transport higher concentrations of Au. Thus, Bisciarelle could represent a segment of a larger fault network that developed from a distinct batch of fluid. This segment was presumably isolated or poorly interconnected with the other segments, similar to what shown in other orogenic deposits (Garofalo et al. 2002).

## Conclusions

The Bisciarelle fault and the neighbor Au deposits are an example of damage zone-dominated, permeable upper crustal fault zones that experienced an intense interaction with a hydrothermal fluid and that modified substantially their fault rocks and protolith. The final product of such interaction are fault zones whose architectures, textures, and compositions differ substantially from those of typical upper-crustal zones in which cataclasis and comminution take place in fluid-poor conditions. These characteristics are probably typical of epizonal orogenic deposits.

A first result of our work is that the coupled study of protolith alteration and faulting processes defines a coherent dataset that is useful to define the chemical and mineralogical modification of a protolith, the fault architecture, and the genesis of fault-hosted mineralizations. We show that the mineralogical and chemical compositions of fault rocks and wallrock may depend critically on which — and to which degree — chemical components are transferred from the fault fluid to the protolith (and vice versa) during deformation.

The mechanism of spherulite growth is probably a unique process. Our proposed fast spherulite formation via growth front nucleation, which involves a CO<sub>2</sub>-rich effervescing hydrothermal fluid, implies a close association between spherulites and fault activity and supports the hypothesis that they are syn-kinematic. However, spherulites are new in the geological record, and so is the possibility that hydrothermal fluids within faults may generate undeformed growth structures. The poor documentation of spherulites in field studies suggest that they are either rare, or alternatively, that they received relatively less attention.

**Supplementary information** The online version contains supplementary material available at <https://doi.org/10.1007/s00126-022-01142-y>.

**Acknowledgements** Funding from the Università degli Studi di Bologna and Università degli Studi di Genova are acknowledged. G. Capponi, L. Crispini, and L. Federico are acknowledged for discussions on a previous version of this manuscript. Bodo Hettendorf is thanked for discussions on how to improve data presentation. Many thanks are due to Alfons Berger, Nick Oliver, and the chief editor for their constructive reviews that helped to significantly improve this article.

**Funding** Open access funding provided by Alma Mater Studiorum - Università di Bologna within the CRUI-CARE Agreement.

## Declarations

**Conflict of interest** All authors declare no competing interests.

**Open Access** This article is licensed under a Creative Commons Attribution 4.0 International License, which permits use, sharing, adaptation, distribution and reproduction in any medium or format, as long as you give appropriate credit to the original author(s) and the source, provide a link to the Creative Commons licence, and indicate if changes

were made. The images or other third party material in this article are included in the article's Creative Commons licence, unless indicated otherwise in a credit line to the material. If material is not included in the article's Creative Commons licence and your intended use is not permitted by statutory regulation or exceeds the permitted use, you will need to obtain permission directly from the copyright holder. To view a copy of this licence, visit <http://creativecommons.org/licenses/by/4.0/>.

## References

- Akinfiyev NN, Diamond LW (2009) A simple predictive model of quartz solubility in water–salt–CO<sub>2</sub> systems at temperatures up to 1000 °C and pressures up to 1000 MPa. *Geochimica et Cosmochimica Acta* 73:1597–1608. <https://doi.org/10.1016/j.gca.2008.12.011>
- Andreassen J-P, Flaten EM, Beck R, Lewis AE (2010) Investigations of spherulitic growth in industrial crystallization. *Chem Eng Res Des* 88:1163–1168. <https://doi.org/10.1016/j.cherd.2010.01.024>
- Bénézech P, Berninger U-N, Bovet N, Schott J, Oelkers EH (2018) Experimental determination of the solubility product of dolomite at 50–253 °C. *Geochimica et Cosmochimica Acta* 224:262–275. <https://doi.org/10.1016/j.gca.2018.01.016>
- Berger A, Herwegh M (2019) Cockade structures as a paleo-earthquake proxy in upper crustal hydrothermal systems. *Scientific Reports* 9:9209. <https://doi.org/10.1038/s41598-019-45488-2>
- Bons PD, Elburg MA, Gomez-Rivas E (2012) A review of the formation of tectonic veins and their microstructures. *J Struct Geol* 43:33–62
- Burger M et al (2015) High-speed, high-resolution, multielemental LA-ICP-TOFMS imaging: Part II Critical Evaluation of Quantitative Three-Dimensional Imaging of Major, Minor, and Trace Elements in Geological Samples. *Anal Chem* 87:8259–8267. <https://doi.org/10.1021/acs.analchem.5b01977>
- Caine JS, Evans JP, Forster CB (1996) Fault zone architecture and permeability structure. *Geology* 24:1025–1028. [https://doi.org/10.1130/0091-7613\(1996\)024%3c1025:fzaaps%3e2.3.co;2](https://doi.org/10.1130/0091-7613(1996)024%3c1025:fzaaps%3e2.3.co;2)
- Capponi G, Crispini L (2002) Structural and metamorphic signature of alpine tectonics in the Voltri Massif (Ligurian Alps, North-Western Italy). *Eclogae Geologicae Helvetiae* 95:31–42
- Cathles LM (1991) The importance of vein selvaging in controlling the intensity and character of subsurface alteration in hydrothermal systems. *Econ Geol* 86:466–471
- Cowan EJ (2020) Deposit-scale structural architecture of the Sigma-Lamaque gold deposit, Canada—insights from a newly proposed 3D method for assessing structural controls from drill hole data. *Mineralium Deposita* 55:217–240. <https://doi.org/10.1007/s00126-019-00949-6>
- Cox SF, Knackstedt MA, Braun J (2001) Principles of Structural control on permeability and fluid flow in hydrothermal systems. In: Richards JP, Tosdal RM (eds) *Structural controls on ore genesis*, vol 14. Society of Economic Geologists, pp 1–24
- Dong G, Morrison G, Jaireth S (1995) Quartz textures in epithermal veins, Queensland; classification, origin and implication. *Econ Geol* 90:1841–1856. <https://doi.org/10.2113/gsecongeo.90.6.1841>
- Drummond SE, Ohmoto H (1985) Chemical evolution and mineral deposition in boiling hydrothermal systems. *Econ Geol* 80:126–147
- Federico L, Spagnolo C, Crispini L, Capponi G (2009) Fault-slip analysis in the metaophiolites of the Voltri Massif: constraints for the tectonic evolution at the Alps/Apenne boundary. *Geol J* 44:225–240. <https://doi.org/10.1002/gj.1139>
- Foxford KA, Nicholson R, Polya DA, Hebblethwaite RPB (2000) Extensional failure and hydraulic valving at Minas da Panasqueira, Portugal: evidence from vein spatial distributions, displacements and geometries. *J Struct Geol* 22:1065–1086. [https://doi.org/10.1016/S0191-8141\(00\)00029-8](https://doi.org/10.1016/S0191-8141(00)00029-8)
- Frenzel M, Woodcock NH (2014) Cockade breccia: Product of mineralisation along dilational faults. *J Struct Geol* 68:194–206. <https://doi.org/10.1016/j.jsg.2014.09.001>
- Garofalo PS (2004) Mass transfer during gold precipitation within a vertically extensive vein network (Sigma deposit - Abitibi greenstone belt - Canada). Part II Mass Transfer Calculations. *Eur J Mineral* 16:761–776. <https://doi.org/10.1127/0935-1221/2004/0016-0761>
- Garofalo PS (2012) The composition of Alpine marine sediments (Bündnerschiefer Formation, W Alps) and the mobility of their chemical components during orogenic metamorphism. *Lithos* 128–131:55–72
- Garofalo PS, Matthäi SK, Heinrich CA (2002) Three-dimensional geometry, ore distribution, and time-integrated mass transfer through the quartz-tourmaline-gold vein network of the Sigma deposit (Abitibi belt - Canada). *Geofluids* 2:217–232
- Genna A, Jébrak M, Marcoux E, Milési JP (1996) Genesis of cockade breccias in the tectonic evolution of the Cirotan epithermal gold system West Java. *Can J Earth Sci* 33:93–102. <https://doi.org/10.1139/e96-010>
- Gibson JM (1988) Principles of Heteroepitaxy. In: Kasper E, Bean JC (eds) *Silicon-molecular beam epitaxy*, vol II. CRC Press, Boca Raton, pp 1–12. <https://doi.org/10.1201/9781351076623>
- Giorza A (2010) Late to post-metamorphic hydrothermalism in the Voltri Unit (Lavagnina Lakes Area, NW Alps). *Structural-Petrological-Geochemical Approach*. PhD, Università degli Studi di Torino
- Goldfarb RJ, Groves DI (2015) Orogenic gold: Common or evolving fluid and metal sources through time. *Lithos* 233:2–26. <https://doi.org/10.1016/j.lithos.2015.07.011>
- Gránásky L, Pusztai T, Tegze G, Warren JA, Douglas JF (2005) Growth and Form of Spherulites Physical Review. *Phys Rev E Stat Nonlin Soft Matter Phys* 72(72):011605
- Gundlach-Graham A et al (2015) High-Speed, high-resolution, multielemental laser ablation-inductively coupled plasma-time-of-flight mass spectrometry imaging: Part I Instrumentation and Two-Dimensional Imaging of Geological Samples. *Anal Chem* 87:8250–8258. <https://doi.org/10.1021/acs.analchem.5b01196>
- Gundlach-Graham A, Garofalo PS, Schwarz G, Redi D, Günther D (2018) High-resolution, quantitative element imaging of an upper crust, low-angle cataclasite (Zuccale Fault, Northern Apennines) by Laser Ablation ICP Time-of-Flight Mass Spectrometry. *Geostand Geoanal Res* 42:559–574. <https://doi.org/10.1111/ggr.12233>
- Halls C, Zhao R (1995) Listvenite and related rocks: perspectives on terminology and mineralogy with reference to an occurrence at Cregganbaun, Co Mayo, Republic of Ireland. *Mineralium Deposita* 30:303–313. <https://doi.org/10.1007/bf00196366>
- Hamilton AR, Campbell KA, Guido DM (2019) Atlas of siliceous hot spring deposits (sinter) and other silicified surface manifestations in epithermal environments. Institute of Geological and Nuclear Sciences, Lower Hutt, N.Z. <https://doi.org/10.21420/BQDR-XQ16>
- Hedenquist JW, Arribas RA, Gonzalez-Urrien E, Hagemann SG, Brown PE (2000) Exploration for epithermal gold deposits In *Gold in 2000*. *Soc Econ Geol* 13:245–277. <https://doi.org/10.5382/Rev.13.07>
- Herrington RJ, Wilkinson JJ (1993) Colloidal gold and silica in mesothermal vein systems. *Geology* 21:539–542. [https://doi.org/10.1130/0091-7613\(1993\)021%3c0539:cgasim%3e2.3.co;2](https://doi.org/10.1130/0091-7613(1993)021%3c0539:cgasim%3e2.3.co;2)
- Jébrak M (1997) Hydrothermal breccias in vein-type ore deposits: a review of mechanisms, morphology and size distribution. *Ore Geol Rev* 12:111–134
- Li J, Ahmed R, Li X (2018) Thermodynamic modeling of CO<sub>2</sub>-N<sub>2</sub>-O<sub>2</sub>-brine-carbonates in conditions from surface to high temperature and pressure energies 11:2627. <https://doi.org/10.3390/en11102627>

- MacLean WH, Kranidiotis P (1987) Immobile elements as monitors of mass transfer in hydrothermal alteration Phelps Dodge Massive Sulfide Deposit, Matagami, Quebec. *Econ Geol* 82:951–962. <https://doi.org/10.2113/gsecongeo.82.4.951>
- McLeish DF, Williams-Jones AE, Vasyukova OV, Clark JR, Board WS (2021) Colloidal transport and flocculation are the cause of the hyperenrichment of gold in nature. *Proc Natl Acad Sci* 118:e2100689118. <https://doi.org/10.1073/pnas.2100689118>
- Moncada D, Mutchler S, Nieto A, Reynolds TJ, Rimstidt JD, Bodnar RJ (2012) Mineral textures and fluid inclusion petrography of the epithermal Ag–Au deposits at Guanajuato, Mexico: Application to exploration. *J Geochem Explor* 114:20–35. <https://doi.org/10.1016/j.gexplo.2011.12.001>
- Neff C, Keresztes Schmidt P, Garofalo PS, Schwarz G, Günther D (2020) Capabilities of automated LA-ICP-TOFMS imaging of geological samples. *J Anal at Spectrom* 35:2255–2266. <https://doi.org/10.1039/D0JA00238K>
- Oliver NHS, Bons PD (2001) Mechanisms of fluid flow and fluid-rock interaction in fossil metamorphic hydrothermal systems inferred from vein-wallrock patterns, geometry and microstructure. *Geofluids* 1:137–162
- Pashley DW (1975) A historical review of epitaxy. In: Matthews JW (ed) *Epitaxial growth*, part A, vol 1. Academic Press, New York USA, pp 2–24
- Pipino G (2001) Le miniere d'oro delle Valli Gorzente e Piota. Ente di Gestione del Parco Naturale di Marcarolo, Bosio (Al)
- Pipino G (1976) Le manifestazioni aurifere del Gruppo di Voltri con particolare riguardo ai giacimenti della Val Gorzente L'Industria Mineraria 11:452–468
- Pipino G (2003) Oro, Miniere, Storia. *Miscellanea di giacimentologia e storia mineraria italiana*. Museo storico dell'oro italiano, 1–220
- Reed MH (1997) Hydrothermal alteration and its relationships to ore fluid composition. In: Barnes HL (ed) *Geochemistry of Hydrothermal Ore Deposits*. Wiley, Third edn, pp 303–365
- Rodriguez-Blanco JD, Sand KK, Benning LG (2017) ACC and Vaterite as intermediates in the solution-based crystallization of CaCO<sub>3</sub>. In: Van Driessche AES, Kellermeier M, Benning LG, Gebauer D (eds) *New perspectives on mineral nucleation and growth. From solution precursors to solid materials*. Springer, Chapter 5, 93–111. <https://doi.org/10.1007/978-3-319-45669-0>
- Rosenberg PE, Holland HD (1964) Calcite-Dolomite-magnesite stability relations in solutions at elevated temperatures. *Science* 145:700–701. <https://doi.org/10.1126/science.145.3633.700>
- Scambelluri M, Rampone E, Piccardo GB (2001) Fluid and element cycling in subducted serpentinite: a trace-element study of the erro-tobbio high-pressure ultramafites (Western Alps, NW Italy). *J Petrol* 42:55–67
- Scarsi M, Malatesta C, Fornasaro S (2018) Lawsonite-bearing eclogite from a tectonic mélange in the Ligurian Alps: new constraints for the subduction plate-interface evolution. *Geol Mag* 155:280–297. <https://doi.org/10.1017/S0016756817000395>
- Scarsi M, Crispini L, Malatesta C, Spagnolo C, Capponi G (2019) Geological Map of a treasure chest of geodiversity: The Lavagnina Lakes Area (Alessandria, Italy). *Geosciences* 9:229
- Seward TM, Williams-Jones AE, Migdisov AA (2014) 13.2 - The Chemistry of metal transport and deposition by ore-forming hydrothermal fluids. In: Holland HD, Turekian KK (eds) *Treatise on Geochemistry (Second Edition)*. Elsevier, Oxford, pp 29–57. <https://doi.org/10.1016/B978-0-08-095975-7.01102-5>
- Sibson RH (1977) Fault rocks and fault mechanisms. *J Geol Soc* 133:191–213. <https://doi.org/10.1144/gsjgs.133.3.0191>
- Sibson RH (2017) Tensile overpressure compartments on low-angle thrust faults Earth. *Planets and Space* 69:113. <https://doi.org/10.1186/s40623-017-0699-y>
- Sibson RH, Robert F, Poulsen KH (1988) High angle reverse faults, fluid pressure cycling, and mesothermal gold-quartz deposits. *Geology* 16:551–555
- Simmons SF, Christenson BW (1994) Origins of calcite in a boiling hydrothermal system. *Am J Sci* 294:361–400
- Spagnolo C, Crispini L, Capponi G (2007) Late structural evolution in an accretionary wedge: insights from the Voltri Massif (Ligurian Alps, Italy). *Geodinamica Acta* 20(1–2):21–35
- Torabi A, Ellingsen TSS, Johannessen MU, Alaei B, Rotevatn A, Chiarella D (2020a) Fault zone architecture and its scaling laws: where does the damage zone start and stop? *Geological Society, London, Special Publications* 496:99–124. <https://doi.org/10.1144/sp496-2018-151>
- Torabi A, Jimenez-Millan J, Jimenez-Espinosa R, Garcia-Tortosa FJ, Abad I, Ellingsen TSS (2020b) Effect of mineral processes and deformation on the petrophysical properties of soft rocks during active faulting. *Minerals* 10:444
- Vignaroli G, Viola G, Diamanti R, Zuccari C, Garofalo PS, Bonini S, Selli L (2020) Multistage strain localisation and fluid-assisted cataclasis in carbonate rocks during the seismic cycle: insights from the Belluno Thrust (eastern Southern Alps, Italy). *J Struct Geol* 141:104216. <https://doi.org/10.1016/j.jsg.2020.104216>
- Whitney DL, Evans BW (2010) Abbreviations for names of rock-forming minerals. *Am Miner* 95:185–187. <https://doi.org/10.2138/am.2010.3371>

**Publisher's note** Springer Nature remains neutral with regard to jurisdictional claims in published maps and institutional affiliations.